Check for updates

Formation of electron-deficient Ni in a Nb/NiFe-layered double hydroxide nanoarray *via* electrochemical activation for efficient water oxidation†

Boyu Ding,‡[a] Zheheng Jiang,‡[a] Xinlong Guo,‡[a] Shukai Wen,[a] Kairui Wang,[a] Shihang Li,[a] Yongqiang Yang,[a] Qihao Sha,[a] Bo Li,[a] Liang Luo, [ID][a] Zhaowang Dan,*[b] Yaping Li [ID] *[a] and Xiaoming Sun [ID] *[a]

The intrinsically sluggish kinetics of the oxygen evolution reaction (OER) at the anode poses a formidable challenge to the industrial application of water electrolysis, although NiFe-based oxides and hydroxides have emerged as promising anodic candidates. Within this framework, we report the synthesis of Nb-doped NiFe-layered double hydroxides (Nb/NiFe-LDH) *via* a straightforward one-step hydrothermal approach. Notably, Nb doping maintained the structural integrity of the NiFe-LDH framework and it enhanced the valence state of the active Ni species during the electrochemical activation process, which accelerated the concomitant reconstruction kinetics of the LDH phase. As a result, Nb/NiFe-LDH demonstrated a remarkable overpotential of 198 mV to attain a current density of 10 mA cm^{-2} in an alkaline electrolyte. This work proposes a novel doping strategy for enhancing the performance of OER electrocatalysts.

1. Introduction

Hydrogen energy, which is regarded as the vanguard of a new generation of energy sources, has attracted significant attention from the scientific community.[1–3] Alkaline water electrolysis, which is known for its high efficiency in hydrogen production,[4,5] does not rely on noble metals or expensive Ti materials.[6,7] However, it is confronted by the significant challenge of high overpotential associated with the oxygen evolution reaction (OER), which impedes the development of alkaline water electrolyzers.[8–10]

In recent years, extensive research has been devoted to the development of low-cost and high-activity OER catalysts.[11–13] Transition metal oxides and hydroxides have shown considerable promise in the OER catalytic process, and NiFe-layered double hydroxide has received wide recognition as a next-generation OER electrocatalyst.[14,15] Applying several optimization strategies, including heteroatom doping,[16–18] strain modulation,[19,20] and vacancy engineering[21,22] to NiFe-LDH can

further promote its OER performance. Furthermore, several studies propose a synergistic interaction between doped atoms and Ni, which activates Ni to a higher valence state during OER,[23,24] and accordingly, converting NiFe-LDH to the active NiFe oxyhydroxide phase is promising in the design and preparation of an excellent NiFe-LDH electrocatalyst for the OER.

In this work, we report the synthesis of an Nb-doped NiFe-LDH nanoarray for oxygen evolution in alkaline medium. High valent Nb^{5+} has a significantly strong ionic polarization force over the oxygen-bridged Ni^{2+}, inducing electron-deficient surroundings and promoting transformation of Ni^{2+} to Ni^{3+} during the OER process. The similar ionic radii of Nb^{5+} and Ni^{2+} helped in maintaining the lattice structural integrity, achieving improvement in both activity and stability of Nb/NiFe-LDH. As a result, Nb/NiFe-LDH required only 198 mV to attain a current density of 10 mA cm^{-2} and sustained it for over 100 hours at 1 A cm^{-2} in an assemble electrolyzer. This strategy not only provides a way to enhance the activity of NiFe-LDH but also offers insights into the design of efficient electrocatalysts for energy conversion and storage applications, potentially laying the groundwork for advancements in renewable energy technologies.

2. Results and discussion

A one-step hydrothermal method was employed to fabricate NiFe-LDH and Nb-doped NiFe-LDH (Nb/NiFe-LDH) electrocata-

[a]*State Key Laboratory of Chemical Resource Engineering, College of Chemistry, Beijing University of Chemical Technology, Beijing 100029, China.*
E-mail: sunxm@mail.buct.edu.cn, liyp@mail.buct.edu.cn
[b]*Ocean Hydrogen Energy R&D Center Research Institute of Tsinghua University in Shenzhen Shenzhen 518057, China. E-mail: danzw@hingear.cn*
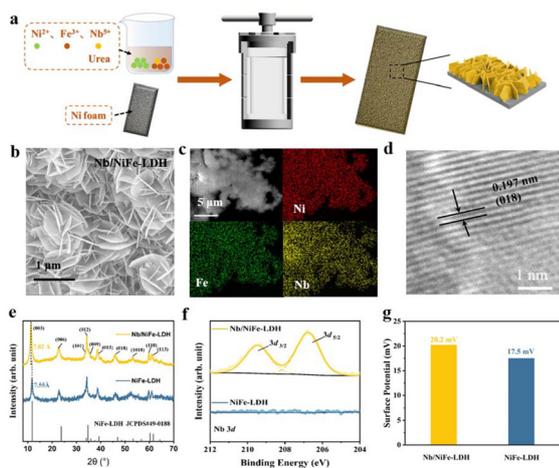
Fig. 1 (a) Schematic of the preparation process of Nb/NiFe-LDH; (b) SEM image of Nb/NiFe-LDH; (c) SEM image and corresponding EDS elemental mapping for Ni, Fe and Nb of Nb/NiFe-LDH; (d) HRTEM image of Nb/NiFe-LDH; (e) XRD patterns of NiFe-LDH and Nb/NiFe-LDH; XPS spectra of (f) Nb 3d for Nb/NiFe-LDH and NiFe-LDH; and (g) zeta potentials of Nb/NiFe-LDH and NiFe-LDH.

lysts on nickel foam (NF), as shown in Fig. 1a. During this procedure, $Ni(acac)_2$ was used as the Ni^{2+} source, and $(acac)^{2-}$ ions in the solvent averted the potential hydrolysis of Nb^{5+}. SEM images in Fig. 1b and ESI Fig. 1† reveal the nanoarray structures of both NiFe-LDH and Nb/NiFe-LDH. The as-synthesized Nb/NiFe-LDH shows an ultrathin two-dimensional (2D) structure. This unique 2D structure is beneficial for the exposure of more Nb/NiFe-LDH active sites and is anticipated to provide hydrophilic and aerophobic properties for the nanoarray. The comparison of these images suggests that Nb^{5+} doping does not induce any significant alteration to the nanostructure of NiFe-LDH. The SEM image and energy-dispersive X-ray spectroscopy (EDS) mapping in Fig. 1c confirm the uniform composition of the catalyst, with homogeneous distribution of Ni, Fe and Nb elements throughout the material. Subsequent X-ray diffraction (XRD) analysis revealed the crystal structure of Nb/NiFe-LDH, as depicted in Fig. 1e. The diffraction peaks are in precise alignment with the reference NiFe-LDH pattern (JCPDS#49-0188), verifying that Nb^{5+} doping does not induce phase segregation or crystallographic structural transformation. Moreover, the (003) diffraction peak observed around 12° indicates a lower diffraction angle for Nb/NiFe-LDH compared to NiFe-LDH, which is directly related to the enlarged basal spacing along the (003) facet, possibly due to a greater amount of anions being contained between the interlayer due to the excessive positive charges in the Nb^{5+}-contained LDH laminates, in keeping the LDH electroneutrality.[25] The HRTEM image in Fig. 1d exhibits a lattice fringe pattern with a spacing of 0.197 nm, which can be indexed to the (018) plane of Nb/NiFe-LDH.

To investigate the chemical composition of LDH and the impact of Nb doping on the electronic structure of LDH, X-ray photoelectron spectroscopy (XPS) analysis was conducted. The

high-resolution Ni 2p XPS spectra in ESI Fig. 2† display peaks at 855.88 eV and 873.48 eV, characteristic of the Ni^{2+} $2p_{3/2}$ and Ni^{2+} $2p_{1/2}$ orbitals, respectively.[26] ESI Fig. 3† presents the high-resolution Fe 2p XPS spectra of NiFe-LDH and Nb/NiFe-LDH. The summary of the Ni 2p and Fe 2p XPS spectra reveals that Nb^{5+} doping does not significantly affect the oxidation states of nickel and iron. The high-resolution Nb 3d XPS spectrum in Fig. 1f demonstrates the presence of characteristic niobium peaks, confirming the successful doping of Nb in its +5-oxidation state.[27]

For NiFe-LDH, Nb^{5+} doping increased the positive charge on the LDH layers. The particles of the two samples were stripped from the NF surface and dispersed in deionized water. As shown in Fig. 1g, the zeta potential of Nb/NiFe-LDH was 20.2 mV, which was 1.15 times higher than that of pure NiFe-LDH (17.5 mV).[28,29] This is attributed to the incorporation of higher-valent Nb, which leads to an increase in the number of positive charges on the surface of the Nb/NiFe-LDH particles, thereby causing an increase in the zeta potential. This finding further confirms the successful incorporation of Nb^{5+}.

To evaluate the performance of Nb/NiFe-LDH, electrochemical measurements were implemented using a three-electrode system in a 1 M KOH electrolyte. Through systematic optimization of Nb doping (ESI Fig. 5†), it was determined that the best OER performance of Nb/NiFe-LDH was achieved at a Nb^{5+} feed amount of 0.15 mmol. This exceptional performance is also evident in Fig. 2a, where Nb/NiFe-LDH requires only 198 mV overpotential to achieve a current density of 10 mA cm^{-2} compared to 285 mV for NiFe-LDH. It should be noted that the NF substrates demonstrated negligible activity
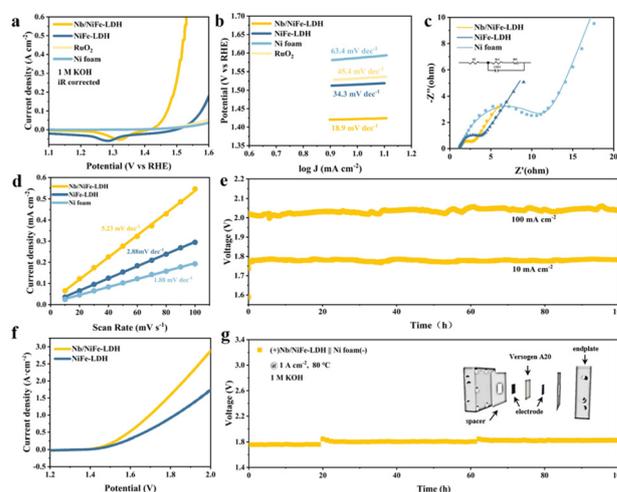

Fig. 2 (a) LSVs and (b) Tafel plots of various samples; (c) Nyquist plots of various samples; (d) plots showing the extracted Cdl value to estimate the ECSA; (e) stability test of Nb/NiFe-LDH at a current density of 0.01 A cm^{-2} and 0.1 A cm^{-2}; (f) LSVs of the AEM electrolyzer using Nb/NiFe-LDH||Ni foam and NiFe-LDH||Ni foam in 1.0 M KOH; and (g) durability test of the AEM electrolyzer using Nb/NiFe-LDH||Ni foam at 1.0 A cm^{-2} in 1.0 M KOH.

(356 mV overpotential @10 mA cm^{-2}) towards OER. Additionally, with a Tafel slope (Fig. 2b) of 18.9 mV per decade, Nb/NiFe-LDH demonstrates much faster reaction kinetics compared to NiFe-LDH (34.3 mV per decade) and Ni foam (63.4 mV per decade), highlighting the beneficial impact of Nb doping on its OER performance. This performance benefit is also observed in the electrochemical impedance spectra (EIS). As shown in Fig. 2c, at a potential of 1.3 V *vs.* RHE, compared to NiFe-LDH (2.653 Ohm) and Ni foam (10.83 Ohm), Nb/NiFe-LDH exhibited the lowest charge transfer resistance of only 1.483 Ohm, signifying the onset of OER at this potential. This provides additional evidence that Nb doping boosts the intrinsic activity of Nb/NiFe-LDH.

Furthermore, cyclic voltammetry measurements at various scan rates (ESI Fig. 6–8†) within the non-faradaic region were performed to obtain the double-layer capacitance (C_{dl}) of the samples, which was subsequently used to evaluate their electrochemical surface area. As shown in Fig. 2d, the C_{dl} of Nb/NiFe-LDH was 5.23 mV dec^{-1}, notably higher than that of NiFe-LDH (2.88 mV dec^{-1}) and Ni foam (1.88 mV dec^{-1}). This accounts for the enhanced current increase rate observed for Nb/NiFe-LDH.

The stability, evaluated in a two-electrode system with nickel foam as the cathode and Nb/NiFe-LDH as the anode, is shown in Fig. 2e. The test was conducted using stepwise chronoamperometry at current densities of 0.01 and 0.1 A cm^{-2}, with each step lasting 100 hours. The results revealed minimal performance degradation, confirming the excellent stability of Nb/NiFe-LDH. Furthermore, to gather operational data for Nb/NiFe-LDH at higher current densities and better match the practical needs of green hydrogen production, the performance of Nb/NiFe-LDH and NiFe-LDH was evaluated using anion exchange membrane (AEM) electrolyzers. It should be noted that the electrolyzers were constructed with Nb/NiFe-LDH or NiFe-LDH as the anode and Ni foam as the cathode, operating at ambient temperature (80 °C). As shown in Fig. 2f, the polarization curves reveal that the electrolyzer with Nb/NiFe-LDH as the anode required just 1.70 V to achieve 1 A cm^{-2}, significantly outperforming the NiFe-LDH electrolyzer, which required 1.82 V. Furthermore, during a continuous 100 hour test at 1 A cm^{-2} (Fig. 2g), the system with Nb/NiFe-LDH as the anode exhibited negligible performance degradation, further underscoring the superior long-term stability of Nb/NiFe-LDH, even at ampere-level current densities.

To elucidate the reasons underlying the superior OER activity of Nb/NiFe-LDH, we performed *in situ* Raman spectroscopy to explore the specific phase evolution of Nb/NiFe-LDH during the OER process, as depicted in Fig. 3b. A peak emerging at approximately 450 cm^{-1} can be ascribed to the vibration of the Ni^{2+}–O bond. It was noted that as the voltage rose to 1.35 V (*vs.* RHE),[29,30] the Ni^{2+}–O bond shifted and transformed into a Ni^{3+}–OOH bond at 456 cm^{-1}. In comparison, the phase transformation from the pre-catalyst metal hydroxide to oxyhydroxide did not occur until 1.37 V for undoped NiFe-LDH (Fig. 3a). The results presented here once again confirm the excellent intrinsic OER activity of Nb/NiFe-
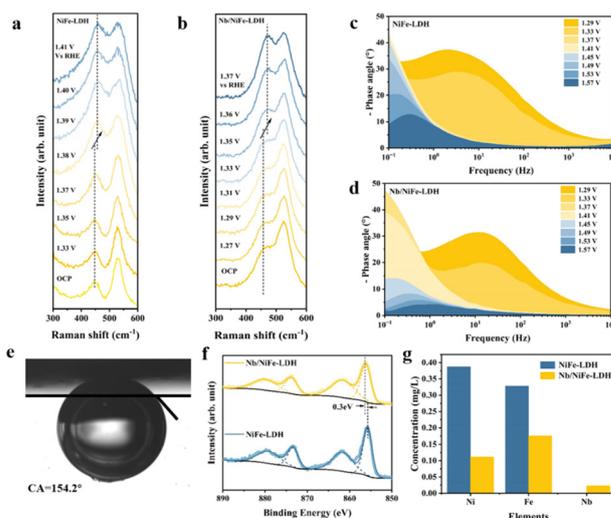

Fig. 3 (a) Operando Raman spectrum of NiFe-LDH, potential range: OCP-1.41 V *vs.* RHE; (b) operando Raman spectrum of Nb/NiFe-LDH, potential range: OCP-1.37 V *vs.* RHE; (c) *in situ* EIS of NiFe-LDH at different potentials; (d) *in situ* EIS of NbNiFe-LDH at different potentials; (e) contact angle of Nb/NiFe-LDH (nanoarrays) with bubble; (f) XPS spectra of Ni 2p for Nb/NiFe-LDH and NiFe-LDH after activation; and (g) ICP results of Nb/NiFe-LDH and NiFe-LDH after the stability test in an electrolyzer for 100 hours.

LDH, also aligning with the electrochemical data. Furthermore, *in situ* electrochemical impedance tests were conducted on both NiFe-LDH and Nb/NiFe-LDH, as shown in Fig. 3c and d. A reduction in the phase angle in the medium-frequency region upon voltage increase indicates that the electrocatalysts are undergoing reconstruction. As the voltage increased from 1.33 V to 1.37 V, the phase angle transited from the medium-frequency to the low-frequency region, signifying the end of reconstruction. This voltage range aligns with that observed in the *in situ* Raman data, attributed to the start of the electrocatalyst reconstruction. In the low-frequency region, the phase angle of Nb/NiFe-LDH dropped more significantly with increasing voltage compared to that for NiFe-LDH, corresponding to the faster OER kinetics of Nb/NiFe-LDH.[31,32] We measured the contact angle of Nb/NiFe-LDH with bubbles in the electrolyte to be 154.2° (Fig. 3e), indicating that our nanoarray material possesses superaerophobic properties. Its exceptionally high current density increase can be attributed to its excellent intrinsic activity and the nanoarray structure. Post-reaction XPS tests were also performed on the electrocatalysts. The Ni 2p peaks of Nb/NiFe-LDH and NiFe-LDH after the reaction are shown in Fig. 3f. A comparison reveals that the peak position of Ni in Nb/NiFe-LDH (856.31 eV) is 0.3 eV higher than that in NiFe-LDH (856.01 eV), indicating that Nb^{5+} doping elevates the valence state of Ni in LDH after the electrochemical test. The XPS results and *in situ* Raman results jointly confirm that the introduction of Nb^{5+} in NiFe-LDH can facilitate the oxidation of Ni and the formation of active oxyhydroxide, thereby resulting in the superior catalytic activity of Nb/NiFe-LDH. The dissolution of metal cations during the

stability test is also a key parameter in monitoring the stability of the electrocatalysts themselves, so Inductively Coupled Plasma Atomic Emission Spectrometry (ICP) testing was carried out using the electrolyte after 100 hours of testing, as shown in Fig. 3g. The leaching of iron and nickel elements in Nb/NiFe-LDH is significantly lower than that in NiFe-LDH, assuring the excellent stability of the Nb/NiFe-LDH catalyst.

To uncover the reasons for the enhanced OER activity of Nb/NiFe-LDH at the atomic level, we conducted DFT calculations to investigate the impact of Nb^{5+} doping on the electronic structure of NiFe-LDH and the OER mechanism. We selected the (011) plane model of Fe-NiOOH as the reaction surface. Initially, charge density difference analysis was employed to reveal the changes in the charge transfer among Ni, Fe, and O after the incorporation of Nb ions, as depicted in Fig. 4a. Observations of the electron depletion surrounding Nb and Ni atoms, coupled with the electron accumulation around the O atoms, indicate that Nb and Ni are present in a high oxidation state. As shown in Fig. 4b, Nb doping induced a finite change in the projected density of states (PDOS) of Nb/Fe-NiOOH compared to pure Fe-NiOOH, particularly near the Fermi level. Subsequently, the d-band centers of the two catalysts were calculated and compared. The results demonstrated that the d-band center of Nb/Fe-NiOOH shifted from −0.635 eV in the original Fe-NiOOH to −0.624 eV, bringing it closer to the Fermi level, which provided a more favorable electronic structure for the adsorption of intermediates. This further confirms that the addition of Nb elevates the d-band center surrounding Ni, leading to improved catalytic activity.

Then, we calculated the free energy of every step for OER (Fig. 4c) for both Nb/Fe-NiOOH and Fe-NiOOH. The results in Fig. 4d show that the rate-determining step of Nb/Fe-NiOOH is the formation of *OOH. This step requires 0.65 eV, which is lower than that of Fe-NiOOH (0.71 eV), confirming the previously experimental results. Taken together, both demonstrate the excellent activity of Nb/Fe-NiOOH after Nb^{5+} doping.

3. Conclusions

This work reports a novel doping candidate, Nb^{5+}, with a similar ionic radius but having a stronger ionic polarization force as compared to Ni^{2+} in NiFe-LDH. The introduction of Nb^{5+} will not induce severe lattice strain or oscillation, which is helpful in maintaining the structural stability of doped NiFe-LDH. Furthermore, the doped Nb upshifts the d band center of Ni (supported by calculation) and facilitates the formation of the NiFe oxyhydroxide active phase (evidenced by *in situ* Raman), delivering an exceptionally low OER overpotential of less than 200 mV at 10 mA cm^{-2}. This work paves new directions for the design and synthesis of next-generation promising OER electrocatalysts in alkaline medium.

Author contributions

X. S., Y. L. and Z. D. conceived and directed the project, supervised the research, and revised the manuscript. B. D., X. G., S. W., B. L., S. L., Y. Y. and K. W. conducted the experiments and wrote the manuscript. Y. L., Q. S. and Z. J. performed DFT calculations. L. L. and X. S. revised the manuscript. All authors discussed the results and commented on the manuscript.

Data availability

The data supporting this article have been included as part of the ESI.†

Conflicts of interest

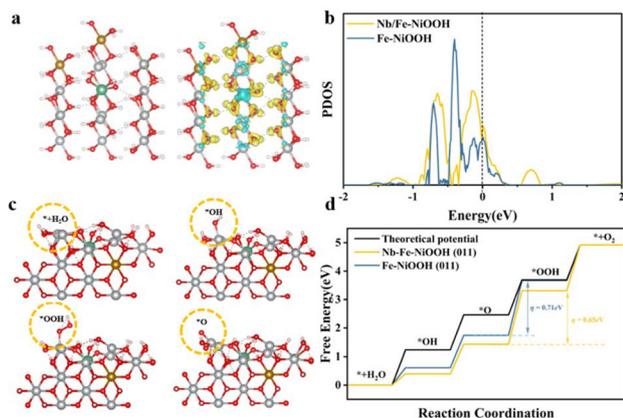There are no conflicts to declare.

Fig. 4 (a) Charge distribution of Nb/Fe-NiOOH. Silver: Ni, brown: Fe, red: O, green: Nb, white: H; (b) projected density of states (PDOS) of Nb/Fe-NiOOH in comparison to undoped Fe-NiOOH; (c) OER schematic pathway on Nb/Fe-NiOOH; and (d) OER free energy diagram of Nb/Fe-NiOOH and Fe-NiOOH.

References

1 N. S. Lewis and D. G. Nocera, *Proc. Natl. Acad. Sci. U. S. A.*, 2006, **103**, 15729–15735.
2 N. T. Suen, S. F. Hung, Q. Quan, N. Zhang, Y. J. Xu and H. M. Chen, *Chem. Soc. Rev.*, 2017, **46**, 337–365.
3 S. Chu and A. Majumdar, *Nature*, 2012, **488**, 294–303.
4 A. S. Emam, M. O. Hamdan, B. A. Abu-Nabah and E. Elnajjar, *Int. J. Hydrogen Energy*, 2024, **64**, 599–625.

5   H. Sun, X. Xu, H. Kim, W. Jung, W. Zhou and Z. Shao, *Energy Environ. Mater.*, 2023, **6**, e12441.

6   L. An, C. Wei, M. Lu, H. Liu, Y. Chen, G. G. Scherer, A. C. Fisher, P. Xi, Z. J. Xu and C. H. Yan, *Adv. Mater.*, 2021, **33**, e2006328.

7   Q. Wang, Y. Cheng, H. B. Tao, Y. Liu, X. Ma, D. S. Li, H. B. Yang and B. Liu, *Angew. Chem., Int. Ed.*, 2023, **62**, e202216645.

8   Z. Y. Yu, Y. Duan, X. Y. Feng, X. Yu, M. R. Gao and S. H. Yu, *Adv. Mater.*, 2021, **33**, e2007100.

9   X. Xie, L. Du, L. Yan, S. Park, Y. Qiu, J. Sokolowski, W. Wang and Y. Shao, *Adv. Funct. Mater.*, 2022, **32**, 2110036.

10 N. Zhang and Y. Chai, *Energy Environ. Sci.*, 2021, **14**, 4647–4671.

11 L. Magnier, G. Cossard, V. Martin, C. Pascal, V. Roche, E. Sibert, I. Shchedrina, R. Bousquet, V. Parry and M. Chatenet, *Nat. Mater.*, 2024, **23**, 252–261.

12 X. Duan, P. Li, D. Zhou, S. Wang, H. Liu, Z. Wang, X. Zhang, G. Yang, Z. Zhang, G. Tan, Y. Li, L. Xu, W. Liu, Z. Xing, Y. Kuang and X. Sun, *Chem. Eng. J.*, 2022, **446**, 136962.

13 H. Xu, C. Zhu, H. Lin, J. Liu, Y. Wu, H. Fu, X. Zhang, F. Mao, H. Yuan, C. Sun, P. Liu and H. Yang, *Angew. Chem., Int. Ed. Engl.*, 2025, **64**, e202415423.

14 Z. Li, G. Lin, L. Wang, H. Lee, J. Du, T. Tang, G. Ding, R. Ren, W. Li, X. Cao, S. Ding, W. Ye, W. Yang and L. Sun, *Nat. Catal.*, 2024, **7**, 944–952.

15 Z. Cai, D. Zhou, M. Wang, S. M. Bak, Y. Wu, Z. Wu, Y. Tian, X. Xiong, Y. Li, W. Liu, S. Siahrostami, Y. Kuang, X. Q. Yang, H. Duan, Z. Feng, H. Wang and X. Sun, *Angew. Chem., Int. Ed.*, 2018, **57**, 9392–9396.

16 Y. Liao, R. He, W. Pan, Y. Li, Y. Wang, J. Li and Y. Li, *Chem. Eng. J.*, 2023, **464**, 142669.

17 X. Wang, Y. Tuo, Y. Zhou, D. Wang, S. Wang and J. Zhang, *Chem. Eng. J.*, 2021, **403**, 162297.

18 P. Li, X. Duan, Y. Kuang, Y. Li, G. Zhang, W. Liu and X. Sun, *Adv. Energy Mater.*, 2018, **8**, 1703341.

19 D. K. Cho, H. W. Lim, A. Haryanto, B. Yan, C. W. Lee and J. Y. Kim, *ACS Nano*, 2024, **18**, 20459–20467.

20 W. Guo, C. Dun, C. Yu, X. Song, F. Yang, W. Kuang, Y. Xie, S. Li, Z. Wang, J. Yu, G. Fu, J. Guo, M. A. Marcus, J. J. Urban, Q. Zhang and J. Qiu, *Nat. Commun.*, 2022, **13**, 1409.

21 Z. Li, D. Wang, J. Xu, H. Sun and Z. Shi, *Chem. Eng. J.*, 2024, **482**, 148858.

22 M. Zubair, P. Kumar, M. Klingenhof, B. Subhash, J. A. Yuwono, S. Cheong, Y. Yao, L. Thomsen, P. Strasser, R. D. Tilley and N. M. Bedford, *ACS Catal.*, 2023, **13**, 4799–4810.

23 F. Dionigi, Z. Zeng, I. Sinev, T. Merzdorf, S. Deshpande, M. B. Lopez, S. Kunze, I. Zegkinoglou, H. Sarodnik, D. Fan, A. Bergmann, J. Drnec, J. F. Araujo, M. Gliech, D. Teschner, J. Zhu, W. X. Li, J. Greeley, B. R. Cuenya and P. Strasser, *Nat. Commun.*, 2020, **11**, 2522.

24 J. Jiang, F. Sun, S. Zhou, W. Hu, H. Zhang, J. Dong, Z. Jiang, J. Zhao, J. Li, W. Yan and M. Wang, *Nat. Commun.*, 2018, **9**, 2885.

25 B. You, M. T. Tang, C. Tsai, F. Abild-Pedersen, X. Zheng and H. Li, *Adv. Mater.*, 2019, **31**, e1807001.

26 Z. Qiu, Y. Ma and T. Edvinsson, *Nano Energy*, 2019, **66**, 104118.

27 M. Zubair, G. Li, B. Wang, L. Wang and H. Yu, *ACS Appl. Energy Mater.*, 2018, **2**, 503–512.

28 C. Qiu, X. Hao, L. Tan, X. Wang, W. Cao, J. Liu, Y. Zhao and Y.-F. Song, *Chem. Commun.*, 2020, **56**, 5354–5357.

29 Z. Lu, J. Wang, P. Zhang, W. Guo, Y. Shen, P. Liu, J. Ji, H. Du, M. Zhao, H. Liang and J. Guo, *Appl. Catal., B*, 2024, **353**, 124073.

30 Y. Zhao, D. P. Adiyeri Saseendran, C. Huang, C. A. Triana, W. R. Marks, H. Chen, H. Zhao and G. R. Patzke, *Chem. Rev.*, 2023, **123**, 6257–6358.

31 B. Chen, P. Hu, F. Yang, X. Hua, F. F. Yang, F. Zhu, R. Sun, K. Hao, K. Wang and Z. Yin, *Small*, 2023, **19**, e2207177.

32 H. Su, W. Zhou, W. Zhou, Y. Li, L. Zheng, H. Zhang, M. Liu, X. Zhang, X. Sun, Y. Xu, F. Hu, J. Zhang, T. Hu, Q. Liu and S. Wei, *Nat. Commun.*, 2021, **12**, 6118.